Hexatic Phase in Covalent Two-Dimensional Silver Iodide

Thuy An Bui [1†], David Lamprecht [1,2†], Jacob Madsen [1], Marcin Kurpas,[3]
Peter Kotrusz,[4,7] Alexander Markevich,[1] Clemens Mangler,[1]
Jani Kotakoski, [1] Lado Filipovic,[2] Jannik C. Meyer,[5]
Timothy J. Pennycook,[6] Viera Skákalová,[1,4,7] Kimmo Mustonen[1*]

[1]University of Vienna, Faculty of Physics, 1090 Vienna, Austria

[2]Institute for Microelectronics, TU Vienna, 1040 Vienna, Austria

[3]University of Silesia in Katowice, 40-00 Katowice, Poland

[4]Danubia NanoTech s.r.o., Bratislava, Slovakia

[5]Eberhard Karls University of Tuebingen, Institute of Applied Physics,

72076 Tuebingen, Germany

[6]University of Antwerp, EMAT, 2020 Antwerp, Belgium

[7]University of West Bohemia, Pilsen, Czech republic

[†]Contributed equally to this work

[*]To whom correspondence should be addressed; E-mail: kimmo.mustonen@univie.ac.at

According to the Kosterlitz-Thouless-Halperin-Nelson-Young (KTHNY) theory, the transition from a solid to liquid in two dimensions (2D) proceeds through an orientationally ordered liquid-crystal-like hexatic phase. While experiments have confirmed the KTHNY melting scenario in some 2D systems such as crystals of skyrmions and of noble gas atoms, no evidence has previously been found for it in covalently bonded 2D crystals. Here, 2D crystals of silver iodide embedded in multi-layer graphene are studied with *in situ* scanning transmission electron microscopy (STEM).

Near the melting point, a highly dynamic state of AgI emerges that we show to be the first observation of the hexatic phase in covalent 2D materials.

First order phase transitions are characterized by a discontinuous change in one or more thermodynamic parameters such as entropy. A common example is ice melting into water accompanied with a transient loss of its structural symmetries. However in the reduced dimensionality of 2D systems, the KTHNY theory (*1–6*) predicts that solid-to-liquid transitions are instead continuous and proceed through an ordered liquid-crystal-like state dubbed as the hexatic phase. In the KTHNY theory the hexatic phase is created by thermally dissociated topological excitations that, over short distances, break down the translational symmetry of a crystal, but which at the same time do not have a significant effect on its orientational coherence (*4*).

The KTHNY theory predictions have been tested at various length scales and with different isotropic physical interactions (*7–14*). Direct real space observations of the 2D solid-to-liquid phase transition have been recorded in macroscopic particle systems such as charged metal spheres (*13*) and colloids (*12*). The hexatic phase has also recently been observed in electronic systems of 2D solids (*15*), including the spin order in magnetic skyrmions (*16*). Atomic crystals, too, have been studied but the observations were limited to noble gases condensed on metal surfaces (*17*) and cesium intercalated into graphite (*18*), both at cryogenic temperatures and studied exclusively via diffraction techniques involving no real space imaging.

However, in all of the above instances (with the notable exception of Ref. 14), weak and omnidirectional force interactions govern the dynamics of the studied systems, standing in contrast to covalent crystals where the chemical bonds are both extremely strong and directionally confined. Given this fundamental difference between covalent and non-covalent crystal systems, it is intriguing to consider whether the KTHNY theory applies to covalent materials with complex chemical structures as implied by simulations with monolayers of (hydrogen bonded) water molecules (*19*). The primary reason this question has remained unresolved until now is the limited thermodynamic stability of 2D

crystals near their melting point, where spontaneous 2D to 3D transformations occur (*20–22*), along with melting temperatures that have exceeded previous experimental limits.

Here we overcome these obstacles with a model system to study the melting mechanism of covalent 2D crystals, consisting of monolayers of 2D silver iodide (AgI) (*23*) encapsulated between graphene layers (*24*), as shown in Figure 1. Encapsulation enables us to observe the dynamic melting of the 2D crystal via time and temperature resolved *in situ* scanning transmission electron microscopy (STEM) by preventing the 2D to 3D transformation of the AgI, and by mitigating radiolysis and knock-on damage (*25*) (see also Figure S4). Furthermore, the non-commensurability of the AgI and graphene lattices ensures the absence of periodic interactions between the two structures, allowing the melting to occur free of significant orientational constraints (see Supplementary Figure S7). From the experimental data we calculate translational and orientational correlations based on atom positions identified in thousands of STEM images using a pre-trained convolutional neural network (CNN), and confirm for the first time the existence of the hexatic phase in covalent materials.

Melting of 2D Crystalline Silver Iodide

Figure 1 shows the evolution of a single encapsulated AgI crystal as it is heated until it melts and then cooled. First, the fully crystalline material transitions into a dynamic crystalline phase, with regions of disorder appearing and disappearing over time. Then, as the material is heated further, the disorder fully takes over. As we will show later, the first stage corresponds to the hexatic phase, and the second stage to the fully liquid phase of the covalent 2D material.

For different 2D AgI crystals, the temperatures of the phase transitions depends on the crystal size (see Supplementary Figure S12) with a possible minor dependence on the encapsulating graphene thickness and crystal orientation. The largest 2D crystals melt at ca. 1200°C, which is substantially higher than the 660°C reported for bulk AgI (*26*). Nevertheless, crystals of all sizes consistently proceed through the two distinct stages of melting, consisting of a dynamically disordering crystalline
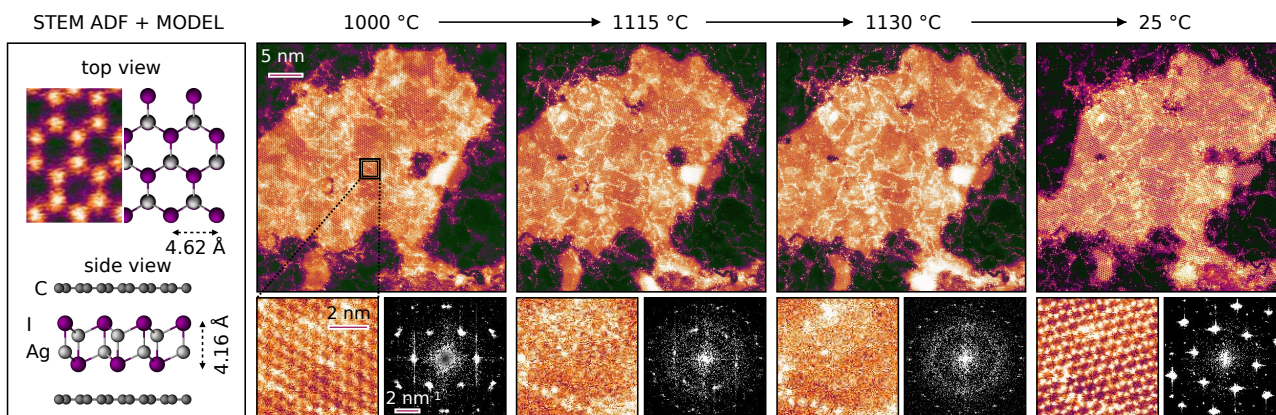
Figure 1: **Melting of 2D crystalline silver iodide** A density functional theory (DFT) model of 2D AgI with an atomically resolved STEM ADF image on the left. Development of the AgI structure during heating and cooling: crystalline state at 1000°C, the phase one of the 2D melting process at 1115°C, and the melting phase two at 1130°C. After cooling down to 25°C, the AgI crystal appears again but is rotated by 12°, on the right end. The Fourier transform images in the bottom row result from 100 rapidly acquired STEM images (see Methods). Additional temperature datapoints and larger field of views can be found from Figure S8-S11.

first stage and a fully disordered second stage, and then fully revert to 2D AgI after the temperature is sufficiently lowered.

The changes occurring in stages one and two are visible both in our real-space images directly as well as in their Fourier transforms (FT, Methods). In the larger crystals, where edge effects are not dominant, and on which we will mostly concentrate here, the first stage generally sets in between 1000°C and 1125°C, and the liquid stage begins to dominate between 1050°C and 1200°C, depending on the crystal size. Close examination of the AgI crystal, shown in Figure 1 at 1115°C, shows regions with clear hexagonal lattice still present, interspersed with areas that appear to lack obvious crystallinity. Note that the encapsulating graphene is not visually apparent in the annular dark field images (ADF, Methods) due to its low atomic number (*27*), but is easily distinguished in the FTs by a set of spots on an outer circle revealing six layers of graphene rotated at different angles in this sample. The graphene layers are essentially unaffected by the temperature changes that in all instances remain far below the melting point of graphene (*28*), as seen through the constant sharpness of its

characteristic spots in the FT of the images.

The disordering seen in the ADF images in stage one is also clearly seen in the FTs, with the 2D AgI crystal spots significantly broadening in the azimuthal (angular) direction. It is important to note that this azimuthal broadening of the 1st-order peaks directly implies the partial loss of orientational order seen in deep hexatic phase materials slightly below the final melting temperature (*17, 29*). This observation is corroborated by the nearly complete loss of the 2nd-order AgI peaks signifying a simultaneous substantial decay of translational order. This state is highly dynamic with the regions of disorder appearing and disappearing over time as captured in the fluctuations in the real-space images shown in Supplementary Video SV1, and similar to phase-fluctuations seen in simulations by Kapfer *et al.* (*30*) and in experiments by Huang *et al.* (*16*). We also emphasize that while the observed fluctuations resemble the critical point fluctuations described by the Ginzburg-Landau (GL) theory, the origin of the fluctuations is different: the GL-transitions are ordinary 2nd-order phase transitions and occur through symmetry breaking involving conventional order parameter behavior (*31*), whereas the Kosterlitz-Thouless (KT) transitions are driven by the binding and unbinding of vortex-antivortex pairs (disclinations), preserving continuous symmetries. Thus, in our case, the fluctuations are likely driven by the instability of the distorted symmetric phase (see the diffraction analysis below), characterized by a reduced Frank's constant (*32*).

At 1130°C the hexagonal AgI crystallinity has completely disappeared, as seen in Figure 1 and Video SV2, indicating that the AgI has become a 2D liquid. It is interesting to note that weak isotropic rings of disordered AgI are still visible in the FT, besides the higher frequency spots of the unaffected graphene layers. However, the fluctuations seen in the lower temperature dynamic phase have disappeared from the FTs, leaving only constant isotropic rings. We attribute this complete loss of orientational order and presence of only a very weak translational order, qualitatively different from the one described before, to the liquid phase. When the temperature is decreased again to 25°C, the 2D AgI crystal structure returns, in this case rotated by 12° with respect to the original lattice orientation,

with sharp spots in the FTs indicating once again the fully crystalline phase.

While direct atomic-resolution images are ideal for probing static and slow enough dynamic configurations, they can only reveal averages of dynamics on shorter timescales. Correspondingly, increasingly large parts of the area are washed out in the real-space images as the temperature is increased, and our information is drawn from the fluctuating sections where structures are still visible intermittently. Therefore, we use nano-beam electron diffraction (NBED) maps (Methods) as a complementary method to analyze the behavior of another relatively large, but somewhat irregular, AgI crystal shown in Figure 2. In the diffraction data, the time averaging takes place in reciprocal space, so that structural correlations can be probed even if the structure reorganizes rapidly, as in a liquid. In the example of Figure 2, when the crystal is brought very close to its final melting point, the left hand side of the AgI flake is in a state that is dynamic on the time scale of single exposures (20 ms), fluctuating between a solid and the phase that we identify as hexatic (Video SV3). The right hand side of the crystal, in contrast, loses its hexagonal structure and continuous rings are visible in the diffraction patterns (Figure 2d, see also Video SV4). These rings are static in the sense that they look the same all over this area and do not change (beyond the noise) in subsequent exposures, and we identify this phase as liquid, as detailed below. The solid phase displays sharp diffraction features of a hexagonal lattice, with a slight asymmetry in the intensities that can be attributed to a small sample tilt as in our previous work (*24*) (Figure 2b). In the hexatic phase, in contrast, we observe azimuthally broadened diffraction peaks, as shown in Figure 2c. This azimuthal broadening is consistent with a lattice that is distorted by a high density of dislocations. Importantly, however, while the orientational order is clearly reduced compared to the crystalline phase, it is nevertheless present and maintained across the entire portion of the crystal that has not transitioned to the liquid state.

The spatial correlation length in liquids is much shorter than in crystalline materials and typically extends no further than a few nearest neighbors. In our diffraction patterns, the complete loss of orientational order is evident from the ring-shaped intensities, which also indicate that the structure is

6

dynamic on a time scale much faster than the diffraction pattern acquisition time. Nevertheless, some insights on the near-ordering can be gained from the radial profile (Figure 2d, see also Figure S13): The primary distances are the same as for crystalline AgI, suggesting that the building blocks and bonding in the liquid phase are the same as in the solid. Compared to crystalline AgI, radial broadening of the peaks can be observed, especially in the 2nd-order diffraction ring of the liquid phase, but also in the measured width of the 1st-order ring (Figure S13). This broadening corresponds approximately to a correlation length between 0.6 and 2 nm, as discussed in the Supplementary Material.
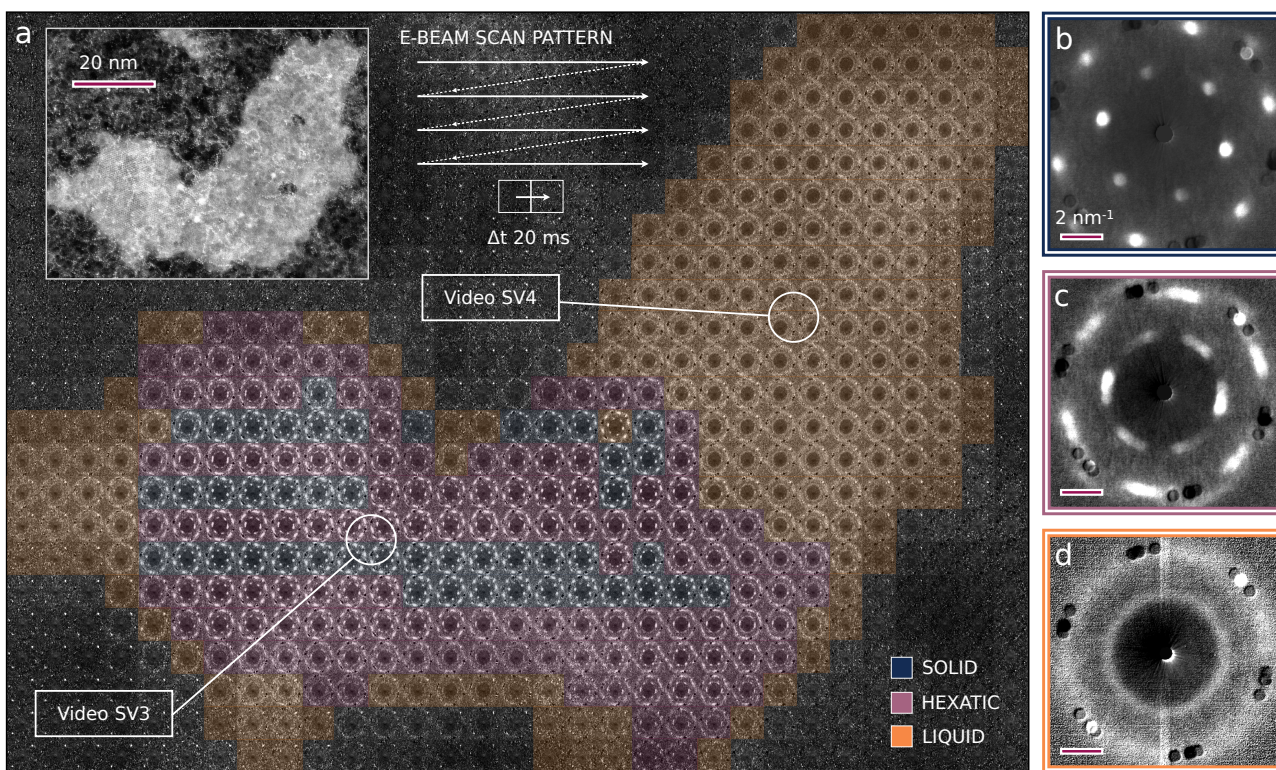
Figure 2: **Phase analysis based on nanobeam electron diffraction (NBED) a** A NBED map of an AgI crystal with its right side in a liquid state and the left side in a dynamic state fluctuating between solid and hexatic phases. The supplementary videos SV3 and SV4 show time series of diffraction patterns recorded on a fixed position as indicated in the figure. **b-d** Diffraction patterns of the solid, hexatic and liquid phases averaged over all diffraction patterns of each phase within the NBED map. The coloring in the NBED map is based on the following classification: sharp diffraction spots → solid phase (blue); azimuthal broadening of the diffraction spots → hexatic phase (purple); isotropic rings → liquid phase (orange).

These observations are not just in excellent qualitative agreement with the theoretical expectations, but as we will show next, also in quantitative agreement. The hexatic phase featuring in the KTHNY melting scenario is rigorously defined by how the translational and orientational orders are correlated as a function of distance within the surrounding material. The theory predicts an exponential decay of the translational correlation within the hexatic phase, distinguishing it from the power-law decay expected in solids at a finite temperature. The hexatic state retains quasi-long range orientational order, distinguishing it from both the crystalline phase and the liquid phase; a fully crystalline phase has a long range orientational order while a liquid phase has only a short range order. These conditions can be expressed in terms of specific critical exponents exactly. The hexatic phase must simultaneously posses a translational correlation power-law decay exponent $\eta_k \geq 1/3$ and an orientational correlation decay exponent $\eta_6 \leq 1/4$ (*11, 33, 34*). These behaviors are demonstrated in Figure 3, as we will now discuss.

Translational Correlation

The translational correlation functions are computed using the center of mass positions r of the AgI polygons detected automatically in real space STEM ADF images by the CNN (see Supplementary Figure S2 and Videos SV5-SV14). Locally, the deviation from the perfect hexagonal crystal is obtained by computing the translational order parameter

$$\Psi_l(r) = e^{-iq_l r}, \tag{1}$$

where q_l is a reciprocal lattice vector of a perfect crystal. The reciprocal lattice vectors are found by first computing a 2D structure factor $S(q)$ (*35*) and then fitting the 1st-order peaks (see Supplementary Material Figure S16 for examples). The translational correlation function is then computed using Ψ_l as

$$G_k(r) = \frac{1}{6} \sum_{l=1}^{6} \frac{1}{N_r} \sum_{i,j}^{N_r} \Psi_l(r_i) \Psi_l^*(r_j). \tag{2}$$

8

The correlation function is averaged over N_r pairs of polygons, and over the first six reciprocal vectors in $S(q)$. Figure 3a shows G_k averaged over all images at each temperature together with the best fitting power-law $\propto r^{-\eta_k}$ and exponential $\propto e^{-r}$ decay functions. The statistical distribution of the power law fitting parameter η_k of all recorded images can be found in Figure 3c.

Power-law decay of $G(k) \propto e^{-\eta_k}$ with low η_k is observed in nearly all images at 1090°C, as expected for a solid system. As the temperature is raised the power law fitting exponent remains nearly constant and well below the critical value of $\eta_k = 1/3$ required by the definition of the hexatic phase until 1120°C. However, at 1125°C the decay of the averaged translational correlation function suddenly becomes quasi-exponential and η_k exceeds 1/3 in more than half of the recorded images, as the material fluctuates between crystallinity and the hexatic state as shown in video SV7.

The KTHNY theory predicts that the solid-hexatic transition is accompanied by the appearance of isolated 5-7 type defects (dislocations), whereas the hexatic-liquid transition is catalyzed by unbounding of the 5-7 defects into isolated 5- and 7-membered rings (disclinations). Here, the abundance of paired and isolated 5-7 defects, segmented via Voronoi tessellation, remain constant across all temperatures until the solid-to-hexatic transition at 1125°C, beyond which the abundance exhibits a rapid increase. A detailed discussion of this analysis is provided in the Supplementary Material, with the results summarized in Figure S14.

With increasing temperature the average η_k rises steadily until it reaches a plateau at around 1150°C, where nearly all images have a translational decay parameter larger than 1/3, indicating a nearly complete loss of translational order with an exponentially falling average G_k. As G_k decays exponentially in both the hexatic and liquid phase, power-law fits are not strictly applicable, leading to a wide spread in η_k. However, the key point is that the decay parameter remains larger than the critical 1/3 value in most recorded images, implying the presence of either the hexatic phase or a semi-ordered liquid. At 1160°C two thirds of the images have no discernible first order diffraction spots, indicating the 2D crystal is almost completely in the liquid state.
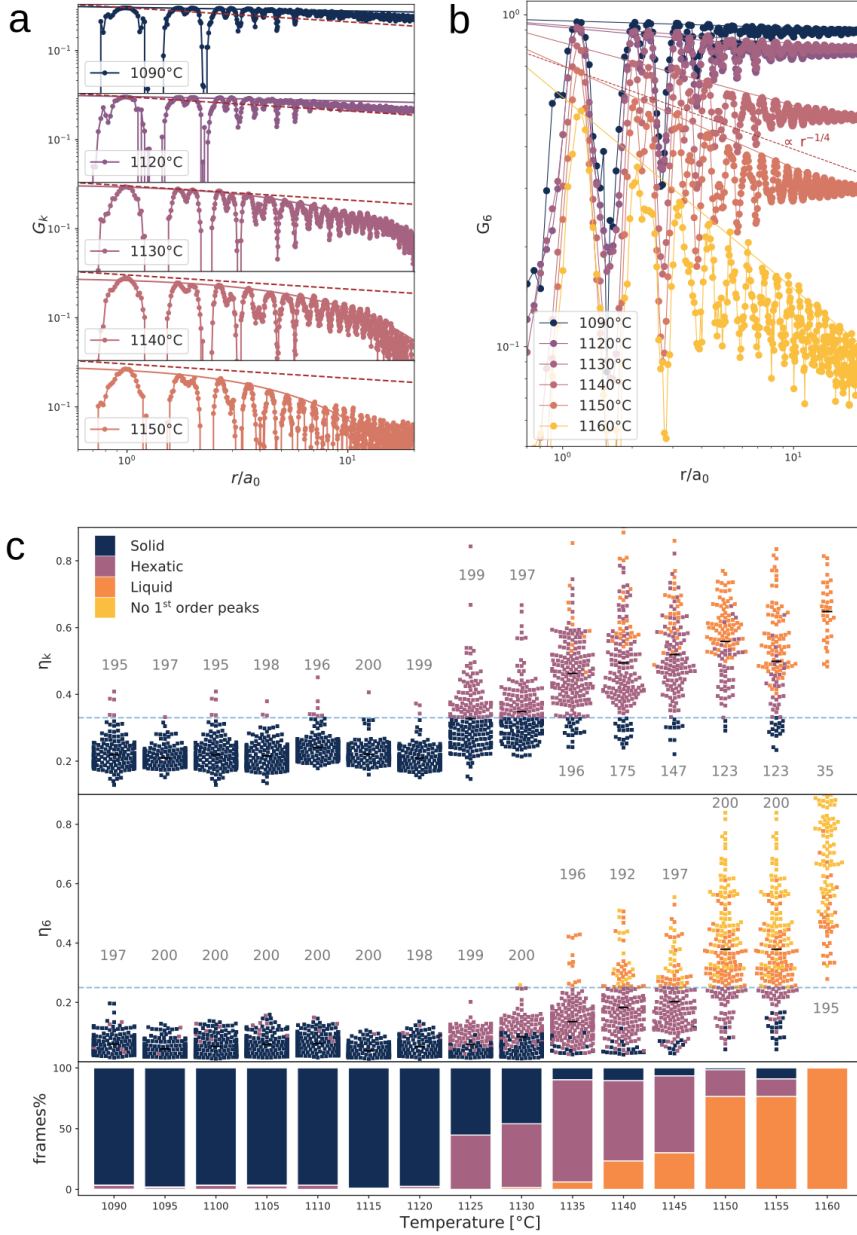
Figure 3: **Spatial correlation functions a** The average translational correlation function $G(k)$ at various temperatures with solid lines indicating either power-law fits (1090°C and 1120°C) or exponential fits (1130°C, 1140°C, and 1150°C). The critical exponent $\eta_k \to 1/3$ is shown as brown dashed lines. **b** The average orientational correlation function $G(6)$ with solid power-law fits. The critical exponent $\eta_6 \to 1/4$ is plotted with brown dashed lines. As negative values can not be plotted in a log-log coordinate system, some datapoints in a and b are not visible. **c** Fit parameters for $G(k)$ and $G(6)$ as a function of temperature for every datapoint. Data are classified and color-coded as: solid phase ($\eta_k \leq 0.33$), hexatic phase ($\eta_k > 0.33$ and $\eta_6 < 0.25$), and liquid phase ($\eta_6 > 0.25$). Relative phase abundances are shown below. All images lacking reciprocal lattice vectors are considered liquid. The number above or below the individual columns indicates the number of analyzed frames.

10

Orientational Correlation

To distinguish the hexatic from solid and liquid phases we must also assess the orientational order which is accounted for by analyzing the orientational correlation

$$G_6(r) = \frac{1}{N_r} \sum_{i,j}^{N_r} \Psi_6(r_i) \Psi_6^*(r_j) \tag{3}$$

in which the local orientational order parameter is defined as

$$\Psi_6(r_i) = \frac{1}{N_{nn}} \sum_{j=1}^{N_{nn}} e^{i6\theta_{ij}}, \tag{4}$$

where θ_{ij} is the angle between a polygon at position r_i and its N_{nn} nearest neighbors relative to a fixed axis. The nearest neighbors are determined by Voronoi tessellation (*35*). Figure 3b shows G_6 averaged over all images at each temperature and the corresponding fits on a log-log scale. The statistics of the power law fitting parameter η_6 among all images can be found in Figure 3c.

During the heating experiments, G_6 remains nearly constant up to 1120°C as expected for a solid. As the temperature is increased to around 1125°C, the orientational correlation G_6 enters into a power law decay $\propto e^{-\eta_6}$, corresponding to a linear decrease on the log-log scale. However, the decay parameters η_6 remain low and do not exceed the critical value $\eta_k = 1/4$ for the hexatic-liquid transition until approximately 1145°C. Nevertheless, even at 1145°C, over 75% of the images display orientational decay consistent with the hexatic phase, i.e., with $\eta_6 < 1/4$. This means that both the orientational order and translational order correlations agree with the definition of the hexatic phase between approximately 1125 and 1145°C.

At 1150°C a sudden increase in η_6 occurs, accompanied by a large deviation in the fitting parameter values, consistent with an increasingly liquid character of the crystal. At these temperatures a sudden increase in the density of isolated 5- and 7-defects is also visible (see supplementary Figure S14). At 1160°C the orientational correlation vanishes completely, and the AgI crystals can be considered molten with an average η_6 of 1.12. These observations are in perfect agreement with the

11

FTs of the datasets shown in supplementary Figure S18, which display a gradual azimuthal broadening of the AgI peaks above 1125°C.

Conclusions

We have, for the first time, recorded the phase transitions from solid to liquid in a covalently bonded 2D crystal, and demonstrated that melting occurs via a hexatic intermediary phase. Graphene encapsulation enabled us to observe this transition in 2D AgI via time and temperature resolved *in-situ* atomic resolution STEM imaging and nano-beam electron diffraction. The hexatic phase, which is only expected in 2D-systems, displays long-range orientational order but only short-range translational order, and occurs within a 25°C temperature interval below the crystal melting point with the absolute temperature of the phase transition varying depending on crystal size. These observations are in excellent agreement with the KTHNY theory, both qualitatively and quantitatively in terms of correlation functions, and extend our understanding of unique 2D melting behavior to strongly bonded covalent crystals with directional bonding and high melting temperatures, far beyond the previously confirmed parameter range.

Acknowledgments

Funding

Authors Contributions

KM and TAB conceived the study. TAB, KM, DL, CM, and VS conducted the experimental work, while DL, KM, TAB, and JM performed the data analysis. PK and VS synthesized the sample material, and MK and AM provided computational support. KM, TJP, DL, JCM, TAB, and VS wrote the manuscript, with contributions from all other authors.

Competing interests

The authors declare no competing interests.

Data and material availability

We declare that all data underlying this study will be made available through University of Vienna PHAIDRA repository upon acceptance of the manuscript.

References

1. J. M. Kosterlitz, D. J. Thouless, *Journal of Physics C: Solid State Physics* **5**, L124 (1972). IOPscience.

2. J. M. Kosterlitz, D. J. Thouless, *Journal of Physics C: Solid State Physics* **6**, 1181 (1973). IOPscience.

3. B. I. Halperin, D. R. Nelson, *Physical Review Letters* **41**, 121 (1978). Publisher: American Physical Society.

4. D. R. Nelson, B. I. Halperin, *Physical Review B* **19**, 2457 (1979). Publisher: American Physical Society.

5. A. P. Young, *Physical Review B* **19**, 1855 (1979). Publisher: American Physical Society.

6. I. Guillamón, *et al.*, *Nature Physics* **5**, 651 (2009). Publisher: Nature Publishing Group.

7. R. Geer, *et al.*, *Nature* **355**, 152 (1992). Publisher: Nature Publishing Group.

8. R. Viswanathan, L. L. Madsen, J. A. Zasadzinski, D. K. Schwartz, *Science* **269**, 51 (1995). Publisher: American Association for the Advancement of Science.

9. C.-F. Chou, A. J. Jin, S. W. Hui, C. C. Huang, J. T. Ho, *Science* **280**, 1424 (1998). Publisher: American Association for the Advancement of Science.

10. E. V. Vasilieva, O. F. Petrov, M. M. Vasiliev, *Scientific Reports* **11**, 523 (2021). Publisher: Nature Publishing Group.

11. K. Zahn, R. Lenke, G. Maret, *Physical Review Letters* **82**, 2721 (1999). Publisher: American Physical Society.

12. C. A. Murray, D. H. Van Winkle, *Physical Review Letters* **58**, 1200 (1987). Publisher: American Physical Society.

13. X. H. Zheng, R. Grieve, *Physical Review B* **73**, 064205 (2006). Publisher: American Physical Society.

14. A. Pasupalak, L. Yan-Wei, R. Ni, M. P. Ciamarra, *Soft Matter* **16**, 3914 (2020). Publisher: The Royal Society of Chemistry.

15. T. Domröse, *et al.*, *Nature Materials* **22**, 1345 (2023). Publisher: Nature Publishing Group.

16. P. Huang, *et al.*, *Nature Nanotechnology* **15**, 761 (2020). Publisher: Nature Publishing Group.

17. T. F. Rosenbaum, S. E. Nagler, P. M. Horn, R. Clarke, *Physical Review Letters* **50**, 1791 (1983). Publisher: American Physical Society.

18. R. Clarke, N. Caswell, S. A. Solin, P. M. Horn, *Physica B+C* **99**, 457 (1980). Publisher: Elsevier.

19. V. Kapil, *et al.*, *Nature* **609**, 512 (2022). Publisher: Nature Publishing Group.

20. H. Inani, *et al.*, *Advanced Functional Materials* **31**, 2008395 (2021). Publisher: Wiley.

21. Y.-T. Tseng, *et al.*, *Small* **18**, 2106411 (2022). Publisher: Wiley.

22. G. Zagler, *et al.*, *2D Materials* **7**, 045017 (2020). Publisher: IOP Publishing.

23. S. Haastrup, *et al.*, *2D Materials* **5**, 042002 (2018). Publisher: IOP Publishing.

24. K. Mustonen, *et al.*, *Advanced Materials* **34**, 2106922 (2022). Publisher: Wiley.

25. R. Zan, *et al.*, *ACS Nano* **7**, 10167 (2013). Publisher: American Chemical Society.

26. S. Hull, D. A. Keen, *Physical Review B* **59**, 750 (1999). Publisher: American Physical Society.

27. O. L. Krivanek, *et al.*, *Nature* **464**, 571 (2010). Publisher: Nature Publishing Group.

28. K. V. Zakharchenko, A. Fasolino, J. H. Los, M. I. Katsnelson, *Journal of Physics: Condensed Matter* **23**, 202202 (2011).

29. I. A. Zaluzhnyy, *et al.*, *Physical Review E* **91**, 042506 (2015). Publisher: American Physical Society.

30. S. C. Kapfer, W. Krauth, *Physical Review Letters* **114**, 035702 (2015). Publisher: American Physical Society.

31. A. Onuki, *Phase Transition Dynamics* (Cambridge University Press, Cambridge, 2002).

32. P. Keim, G. Maret, H. H. von Grünberg, *Physical Review E* **75**, 031402 (2007). Publisher: American Physical Society.

33. V. M. Bedanov, G. V. Gadiyak, Y. E. Lozovik, *Physics Letters A* **109**, 289 (1985). Publisher: Elsevier.

34. E. P. Bernard, W. Krauth, *Physical Review Letters* **107**, 155704 (2011). Publisher: American Physical Society.

35. V. Ramasubramani, *et al.*, *Computer Physics Communications* **254**, 107275 (2020). Publisher: Elsevier.

36. J. Madsen, T. Susi, *Open Research Europe* **1** (2021).

37. P. Giannozzi, *et al.*, *J. Phys.: Condens. Matter* **21**, 395502 (2009). Publisher: IOP Publishing.

38. P. Giannozzi, *et al.*, *Journal of Physics: Condensed Matter* **29**, 465901 (2017). Publisher: IOP Publishing.

39. J. P. Perdew, K. Burke, M. Ernzerhof, *Phys. Rev. Lett.* **77**, 3865 (1996). Publisher: American Physical Society.

40. D. R. Hamann, *Phys. Rev. B* **88**, 085117 (2013). Publisher: American Physical Society.

41. P. Scherpelz, M. Govoni, I. Hamada, G. Galli, *J. Chem. Theory Comput.* **12**, 3523 (2016). Publisher: American Chemical Society.

42. S. Grimme, *J. Comput. Chem.* **27**, 1787 (2006). Publisher: Wiley.

43. V. Barone, *et al.*, *J. Comput. Chem.* **30**, 934 (2009). Publisher: Wiley.

44. H. J. Monkhorst, J. D. Pack, *Phys. Rev. B* **13**, 5188 (1976). Publisher: American Physical Society.

45. M. Weiler, G. Cesa, *Advances in Neural Information Processing Systems* (Curran Associates, Inc., 2019), vol. 32. Publisher: Morgan Kaufmann Publishers Inc.

46. A. Trentino, *et al.*, *Nano Letters* **21**, 5179 (2021). Publisher: American Chemical Society.

47. T. Susi, J. C. Meyer, J. Kotakoski, *Nature Reviews Physics* **1**, 397 (2019). Publisher: Nature Publishing Group.

48. M.-Y. Ma, *et al.*, *Materials Today Nano* **22**, 100304 (2023). Publisher: Elsevier.

49. P. Lazić, *Computer Physics Communications* **197**, 324 (2015). Publisher: Elsevier.

50. P. Buffat, J.-P. Borel, *Physical Review A* **13**, 2287 (1976). Publisher: American Physical Society.

51. X. Zhang, *et al.*, *Journal of Physics: Condensed Matter* **31**, 075701 (2018). Publisher: IOP Publishing.

52. P. Digregorio, D. Levis, L. F. Cugliandolo, G. Gonnella, I. Pagonabarraga, *Soft Matter* **18**, 566 (2022). Publisher: The Royal Society of Chemistry.

53. C. Hofer, K. Mustonen, V. Skákalová, T. J. Pennycook, *2D Materials* **10**, 035029 (2023). Publisher: IOP Publishing.

54. Y.-W. Li, M. P. Ciamarra, *Physical Review E* **100**, 062606 (2019). Publisher: American Physical Society.

Supplementary Material:

Materials and Methods

Sample Preparation

The heterostructures of graphene-encapsulated AgI were synthesized using the chemical process detailed in our previous work, where silver nitride served as the metal precursor and iodic acid as the iodine source (*24*). The structures were grown directly on Protochips Fusion heating holders, which were subsequently used for the *in situ* heating experiments. The freestanding portions of the sample were supported by a holey carbon film, mounted on a 200 nm thick silicon nitride/silicon carbide membrane with 10 μ perforations, as shown in Figure S1.
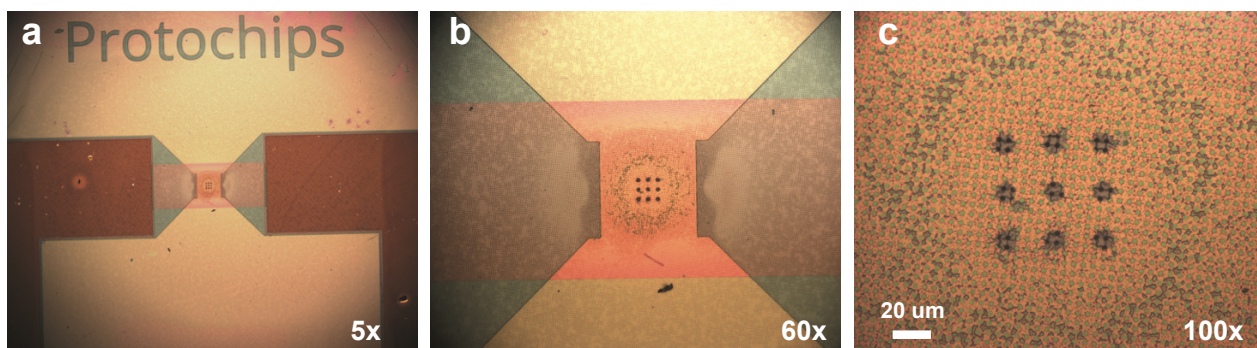
Figure S1: **Optical compound microscope images of a Protochips Fusion heating holder** The graphene encapsulated 2D AgI is suspended on amorphous carbon film, which is supported on a silicon nitride/silicon carbide membrane. The carbon membrane is only visible in panel **c**, whereas the silicon nitride/silicon carbide membrane with a total of nine holes, is visible in lower magnifications images in **a-b** as well.

Scanning Transmission Electron Microscopy (STEM)

All microscopy data in this study were acquired using an aberration-corrected Nion UltraSTEM 100 scanning transmission electron microscope. The experiments were performed at an acceleration voltage of 60 kV and a convergence semiangle of ca. 35 mrad, and the images captured using a high-

angle annular dark-field (HAADF, cited in the manuscript as ADF) detector featuring a collection semi-angle of 80–300 mrad. The electron energy loss spectra in Figure S19 were acquired using a custom-built device comprising a Gatan PEELS 666 spectrometer and an Andor iXon 897 electron-multiplying charge-coupled device (EMCCD) camera with 0.5 eV/px energy dispersion. The Protochips Fusion sample carriers (see above) were resistively heated by a Keithley sourcemeter model 2614B controlled through Protochips Fusion proprietary software. The accuracy of the temperature setpoint provided by the manufacturer is $\pm$ 5%. In these experiments a temperature ramping rate of 6°C per minute was used, and a 15-min thermal stabilization period was allowed before data collection at each temperature setpoint.

STEM Acquisition Parameters

The overviews showing the AgI crystal in Figure 1 were acquired with a pixel dwell time of 8.0 μs using a 2048 $\times$ 2048 probe array. The electron beam's flight-back time was 120 μs per scan line in all experiments, in this case resulting in a total image acquisition time of 33 s. The Fourier transforms shown in Figure 1 were averaged from Fourier transforms of 100 individual STEM ADF images. Each of these images consisted of a 1024 $\times$ 1024 probe array with a pixel dwell time of 0.5 μs. This resulted in a total image acquisition time of 0.65 s. The images used for the spatial correlation function analysis (Figure 3) were acquired with a pixel dwell time of 1.0 μs and a 1024 $\times$ 1024 probe array, resulting in a frame acquisition time of 1.17 s per image. A total of 200 images were captured for each temperature condition. The nano-beam electron diffraction (NBED) patterns (Figure 2 and Supplementary Videos SV3 and SV4) were acquired using a nearly parallel beam illumination mode with an approximate probe size of 5 nm. Each diffraction pattern was recorded with an acquisition time of 20 ms. For the NBED map, a 40 $\times$ 40 probe array was used, with a spatial step size of 1.75 nm. A background subtraction for the NBED images in Figures 2 and S13 was performed by averaging 20 NBED images taken outside the crystal and subtracting this contribution from each diffraction

pattern.

Fourier Transforms

The Fourier transforms shown in Figures 1 and S18 were generated using the ImageJ software suite. This process involved computing a 2D FT for each STEM ADF image (16 nm × 16 nm each) of an image stack containing either 100 (Figure 1) or 200 (Figure S18) individual frames, and subsequently averaging the resulting transforms.

STEM Simulations

The simulated STEM ADF images in Figures S3 and S5 were computed using the *ab*TEM code (*36*). The atomic models used for the simulations were produced via density functional theory (DFT) calculations or convolutional neural network (CNN, see below). All simulations employed realistic instrument parameters: 60 kV acceleration voltage, 80–300 mrad ADF detection semiangle, and 35 mrad probe convergence semiangle. For DFT structures, potential and probe sampling were set to 0.03 Å, using Nyquist sampling for the grid scan, while CNN models used 0.1 Å potential and probe sampling with Nyquist sampling of 0.358 Å. Poisson noise was applied to the simulated images, replicating the experimental electron dose per frame of 1.3×10^4 electrons/Å^2.

Density Functional Theory Modeling

First principles calculations were performed using the plane wave QUANTUM ESPRESSO (QE) package (*37, 38*). We used the Perdew–Burke–Ernzerhof exchange-correlation functional (*39*) as implemented in the full-relativistic SG15 optimized norm-conserving Vanderbilt (ONCV) pseudopotentials (*40, 41*). The plane wave basis was converged using the kinetic energy cut-offs 60 Ry and 240 Ry for the wave function and charge density, respectively. The two-dimensional heterostructure was modeled by introducing a vacuum 17.8 Å in the stacking (z-) direction minimizing the interaction between the periodic images of the system. Van der Waals interactions were taken into account

20

within the semi-empirical Grimme's DFT-D2 corrections (*42, 43*). Self-consistency was achieved using $10 \times 10 \times 1$ Monkhorst-Pack (*44*) k-point mesh for the supercell calculations. The optimized lattice constant of AgI, $a_{\text{AgI}} = 4.59$ Å, was found by variable cell relaxation, assuming force and total energy thresholds 10^{-4} Ry/bohr and 10^{-5} Ry respectively, and allowing the cell to move in the two-dimensional plane.

Obtaining the Atomic Structure from STEM Images

Convolutional Neural Network (CNN)

The CNN was designed for analyzing microscopy images features a UNET architecture with rotational equivariance, based on the approach developed by Weiler *et al.* (*45*). The neural network is specifically trained to detect atoms in simple hexagonal lattices on images with a pixel size of 0.1 Å/px, and images with other pixel sizes are rescaled accordingly. The scaling factor is determined directly from the known AgI lattice vectors using a robust automated algorithm in Fourier space. The image mean and standard deviation are normalized, but in images with significant contamination, the statistics can be heavily skewed due to the contrast difference between the lattice and contamination regions. To address this, we apply the neural network in two stages: in the first pass, we generate a segmentation map to create a mask that excludes heavily contaminated areas from the statistics (note however that high-contrast contamination areas in our data still in many cases contain sufficient information to interpret the most likely atom positions). The second pass then uses these contamination-masked images with improved normalization for the final prediction. While this process could be iterated until convergence, we find that two passes are typically sufficient. The full description of the CNN architecture used for this work can be found in Ref. 46.

In our workflow (Figure S2), the CNN output is first converted into a point map representing all discernible atoms within the image area. For validation, this atom position map can also generate a simulated image of the initial structure, as shown in Figure S3. The stable Delaunay algorithm is then
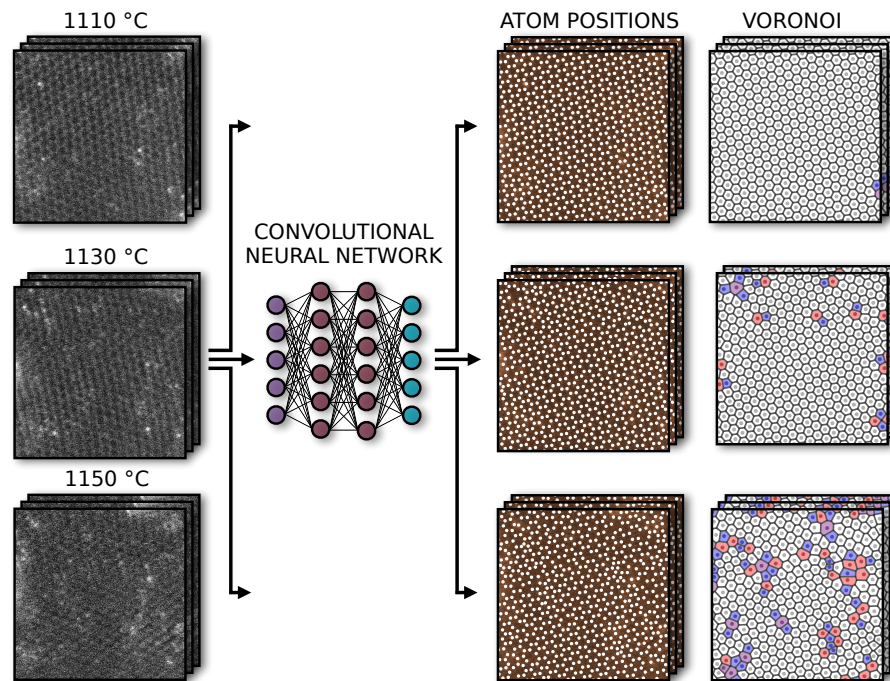
Figure S2: **Segmentation workflow** STEM ADF input stacks are analyzed automatically using a convolutional neural network (CNN) to detect the most probable atom positions in each frame. To study the defect configurations and polygon orientations, the polygon center of mass is first determined using the stable Delaunay algorithm, and the configurations are segmented further by applying Voronoi tessellations. The example STEM images have a field of view of 7.4 nm × 7.4 nm.

applied to determine the center of mass of each polygon defined by the atoms, which is subsequently used for Voronoi tessellation (*35*), as shown on the right in Figure S2. To mitigate image distortions caused by electron-beam flight-back on the left edge, and uncertainties related to atom positions next to the image boundaries, we discard a ca. 1 nm wide slice around the image perimeter (see e.g. Figure S3a). The spatial correlation functions are computed from the tessellated region that excludes the edges.

Baseline Behavior of Spatial Correlation Functions

Electron-beam-induced damage in 2D materials typically arises from knock-on displacement, radiolysis, or thermal effects, leading to vacancies, bond-breaking, or structural modifications (*47*). Persistent
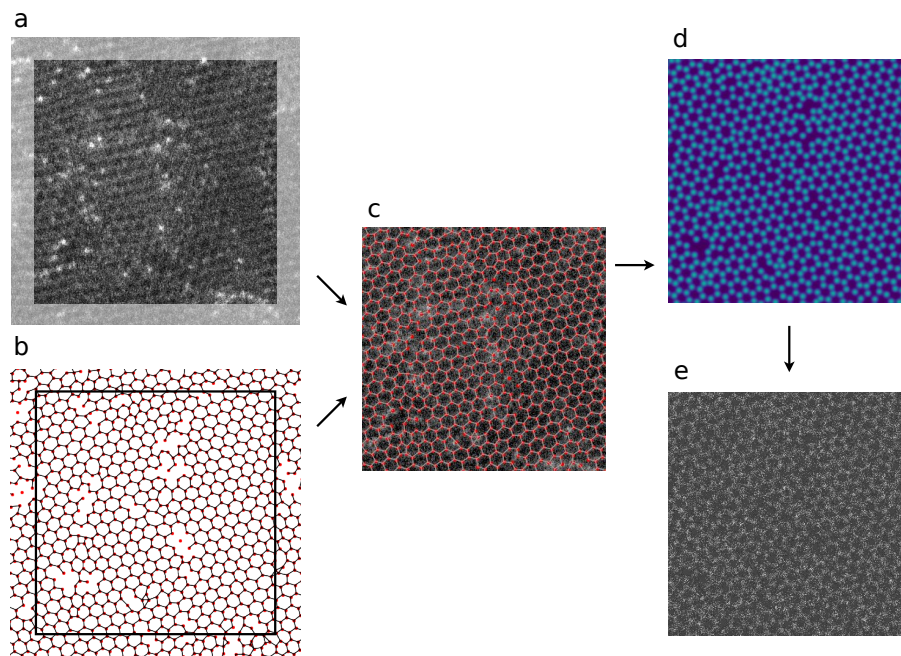
Figure S3: **Comparison of the extracted atomic structure and the original STEM image a** Original STEM ADF image. **b** Delaunay wire mesh based on the CNN output with atom positions marked with red dots. **c** The original STEM image overlaid with the wire mesh. Simulated STEM ADF image of the extracted atomic structure in **d** without noise and with a $\sigma = 0.6$ Gaussian filter, and in **e** with realistic acquisition-related Poisson noise.

strain from such defects perturbs the crystal, causing a decay in its spatial correlations. However, it is generally accepted that graphene encapsulation can very effectively mitigate such damage (*25*). This is also evidenced by the baseline dataset acquired in our experiments to track the temporal evolution of spatial correlations during electron irradiation. This dataset comprises 952 continuously acquired STEM ADF images, with spatial correlation decay exponents computed in Figure S4d. These results clearly indicate that electron irradiation alone does not cause any irreversible changes in the studied structures. The accumulated electron dose during the baseline data collection was approximately 1.45×10^7 electrons/Å^2, with a total data collection time of around 1114 s.

Another source of uncertainty in the estimation of spatial correlations is the random noise arising from thermal instabilities of the sample and holder, as well as rapid AgI structural reordering that we

are unable to fully capture in our experiments. We evaluated the noise tolerance of the CNN by first adding artificial Gaussian noise on the baseline image data, and then re-evaluated the correlation decay exponents frame-by-frame. These results that are summarized in Figure S4d, and show that while the translational decay exponents (η_k) are slightly higher for noisy input data, the overall contribution is not significant even in case of extremely noisy input with a signal-to-noise ratio (SNR) of -75.13 dB. The SNR for STEM ADF images was here calculated as

$$SNR = 10 \cdot \log_{10}\left(\frac{Signal\ Power}{Noise\ Power}\right), \qquad \text{(Eq. S1)}$$

where $Signal\ Power$ is the variance (or mean squared value) of a reference image (e.g. Figure S4a), and $Noise\ Power$ is the variance of the difference between the noisy image and the reference.

CNN Handling of Defects and Lattice Distortions

The CNN used in this work was trained to detect atom positions in simple hexagonal materials. AgI, with its more complex structure comprising two atoms per column (Ag and I), poses challenges due to potential misalignment of the Ag and I atoms due to thermal excitations, which could confuse the CNN. Additionally, the 60 keV electron beam may induce Ag and I vacancies, occasionally with nonzero charge states (*48*), further distorting the AgI lattice. To assess robustness of the CNN against these lattice distortions, the CNN was tested with simulated input data shown in Figure S5. The results indicate that the CNN is able to track the center of mass of even severely misaligned Ag and I atoms, while in case of single atom vacancies, the CNN accurately estimates the position of the remaining I and Ag atoms.
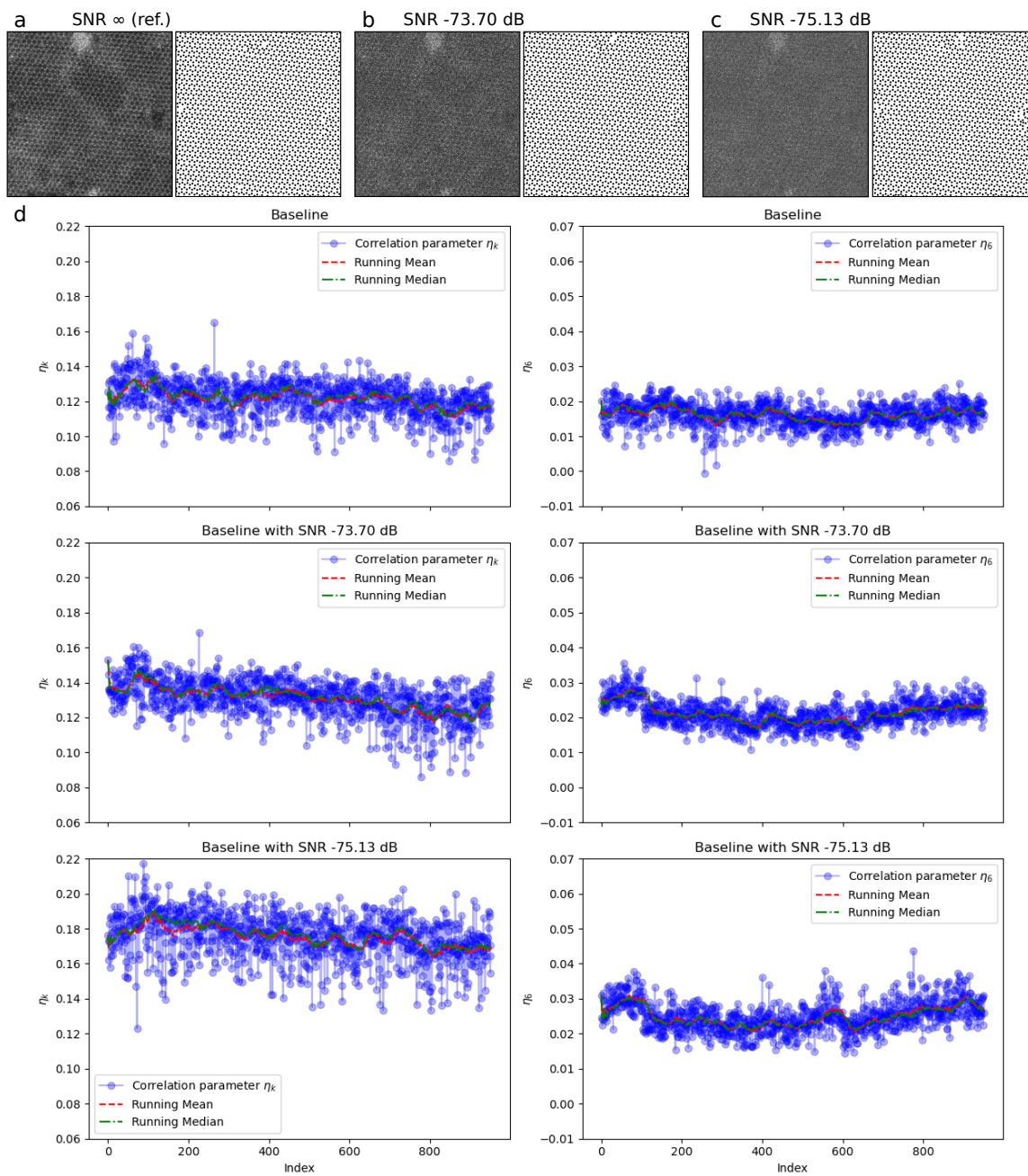
Figure S4: **Baseline of the spatial correlation function decay exponents a** A single image from the baseline dataset with CNN-detected atom positions. **b-c** The same image with added artificial Gaussian noise. **d** Translational (η_k) and orientational (η_6) decay exponents calculated for 952 images, both with and without added Gaussian noise.
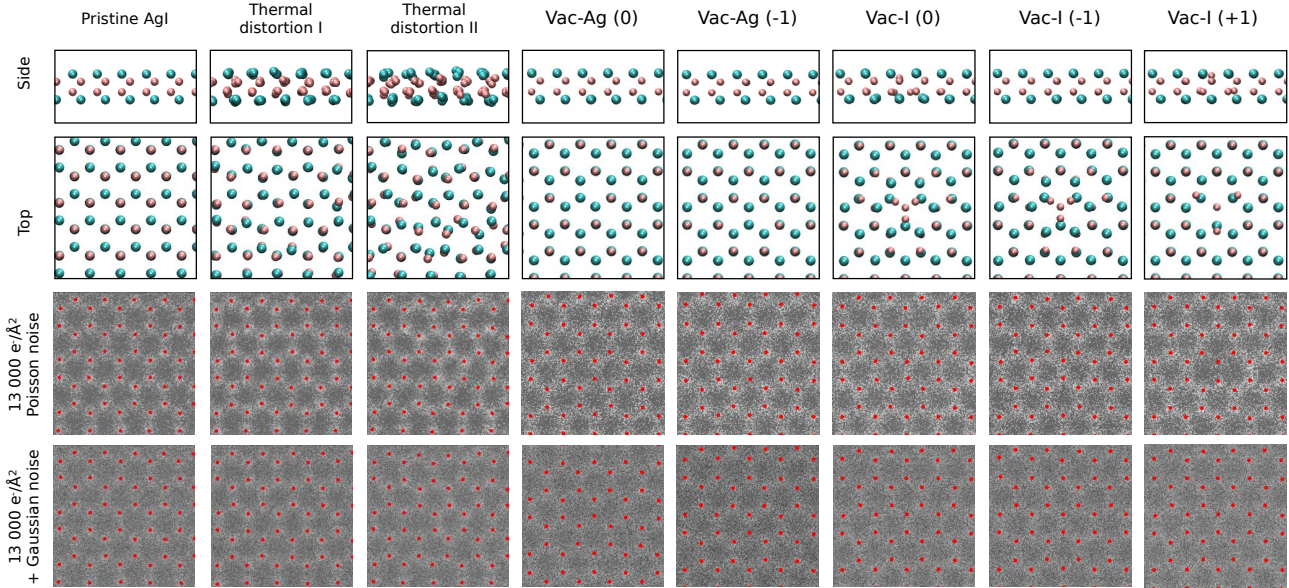
Figure S5: **Atom positions in distorted AgI lattices.** The top row displays thermalized AgI structures without z-directional confinement (imposed experimentally by graphene), distorted by thermal excitations and vacancy-type defects with various charge states (*48*). The middle row presents simulated STEM ADF images computed for realistic electron doses and Poisson noise of approximately 1.3×10^4 electrons/Å^2 per frame, as used in the experiments. The bottom row includes the same images with additional Gaussian noise, approximating the diffuse background from encapsulating graphene layers and the sample's thermal instability.

Graphene-AgI Interaction Strength

Due to the difference in lattice constants, the graphene and AgI lattices are inherently non-commensurate. To estimate the interaction strength between these structures from first principles, we utilized the CellMatch code (*49*) to identify feasible commensurability conditions. This approach enabled the construction of a relatively small supercell containing only 128 atoms, where the AgI layer was sandwiched between graphene layers. In this configuration, the graphene lattice constant was compressed by 1.2% to $a_G = 2.43$ Å, and the AgI layer was twisted by $\theta = 19.1°$ relative to the graphene layers; without the twist and compression the simulation cell would be too large to compute the interaction energies. The final structure is shown in Figure S6.

Within the simulation cell, it is evident that the positions of iodine (I) atoms closest to the graphene

layers exhibit no strong correlation with the carbon atoms. Instead, these iodine atoms are distributed almost equally among the top sites (I atom positioned directly below a carbon atom), bridge sites (I atom located at the midpoint of a C–C bond), and hollow sites (I atom situated at the center of a graphene hexagon). It is therefore anticipated that AgI will exhibit only a weak positional preference relative to the graphene layers. This is confirmed by performing total energy calculations for 36 distinct positions of AgI while keeping the graphene layers fixed. Each configuration is made by shifting the AgI atoms from their initial position shown in Figure S7a by $\delta_x \in [0, 1.2145 \text{ Å}]$, $\delta_y \in [0, 0.7012 \text{ Å}]$. Due to symmetry of graphene lattice we change the position of AgI by (δ_x, δ_y) in the range depicted by the orange rectangle in Figure S7a. For all configurations the interlayer distance is fixed at $d_{\text{inter}} = 3.42$ Å, which corresponds to the average interlayer distance of the fully relaxed structure for $\delta_x = 0$ and $\delta_y = 0$.

The obtained total energy profile $\Delta E = E(\delta_x, \delta_y) - E(0, 0)$ shown in Figure S7b is nearly uniform, indicating that the energy landscape is flat, with a variation of only 1 meV across the entire simulation cell (128 atoms). Considering that the commensurability of the graphene-AgI system in real samples is lower than in our simulations (where compressed graphene ensures commensurability within a cell of approximately 1 nm), it is expected that, in actual samples where graphene layers are randomly oriented and non-compressed, the energy landscape will be even flatter. This directly implies that the AgI crystal is nearly free of orientational constraints, and that the mutual orientation and alignment between AgI and graphene is not important for the melting process.
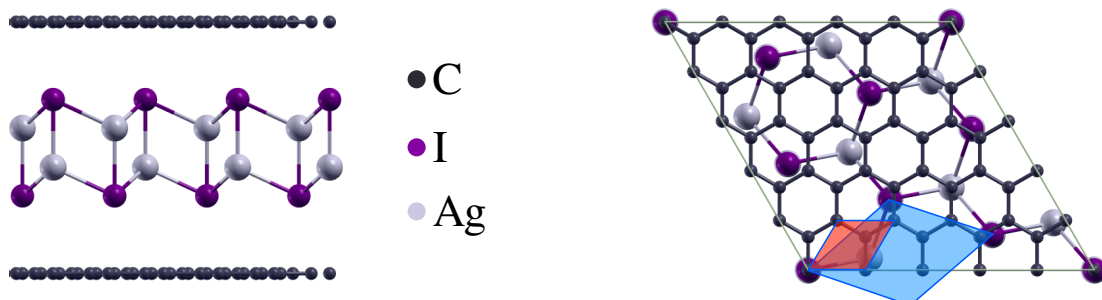
Figure S6: **Atomic structure of two-dimensional AgI encapsulated in graphene sheets.** Side (left panel) and top (right panel) view of the atomic structure with atoms indicated by colors. Red and blue shaded areas depict the primitive unit cells of graphene and AgI lattices, respectively. The relative twist angle between the unit cells is $19.1°$
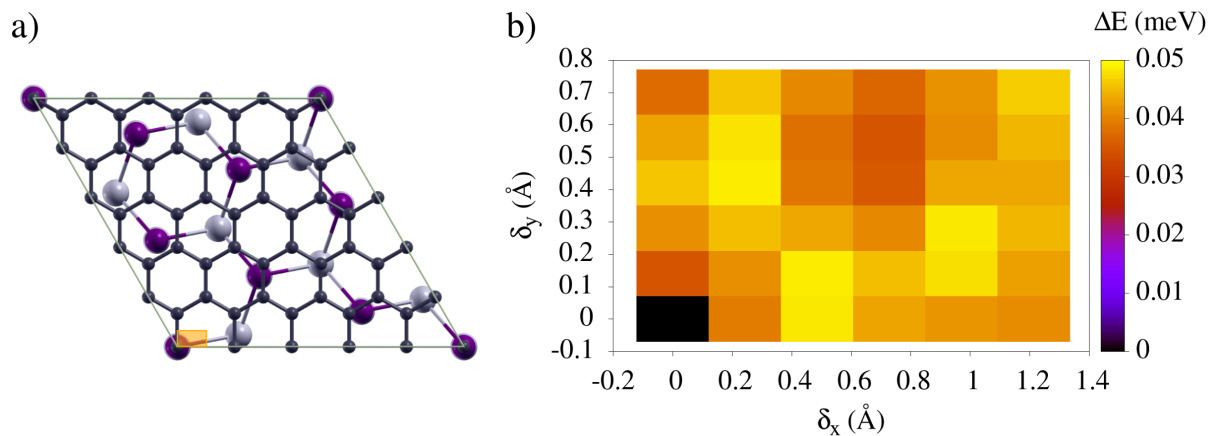
.

Figure S7: **Total energy profile of the G/AgI/G heterostructure under the shift of AgI layer** **a** crystalline structure of G/AgI/G heterostructure. The orange rectangle depicts the range of shifts (δ_x, δ_y) of AgI layer with respect to fixed graphenes. **b** Total energy difference map $\Delta E = E(\delta_x, \delta_y) - E(0,0)$ plotted for 36 positions of AgI obtained by shifting . The δ_x and δ_y are measured from the bottom left corner of the rectangle. $E(0,0) \equiv E(\delta_x = 0, \delta_y = 0)$ is the total energy corresponding to $\delta_x = 0$, $\delta_y = 0$, when the Iodine atom in the bottom left corner of the rectangle sits between two carbon atoms .

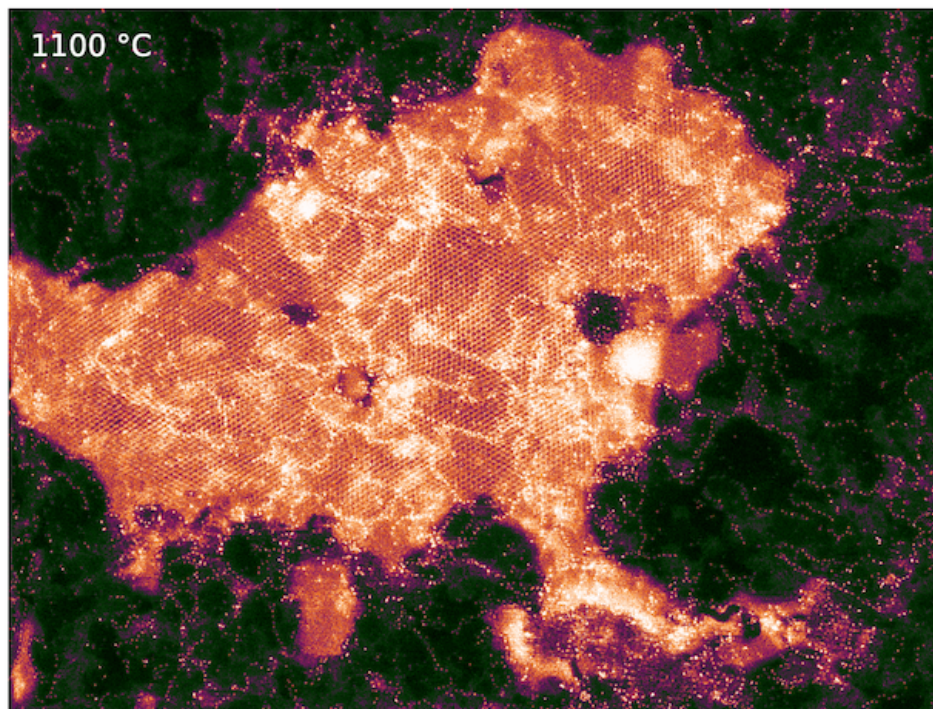# Supplementary Datapoints for Manuscript Figure 1
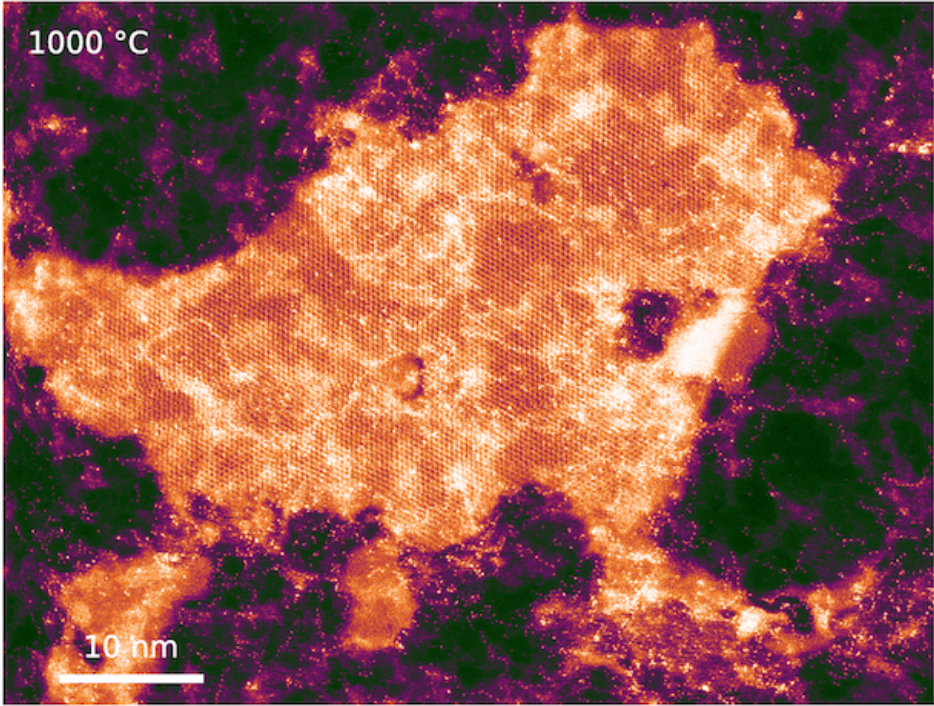
Figure S8: **1000°C**
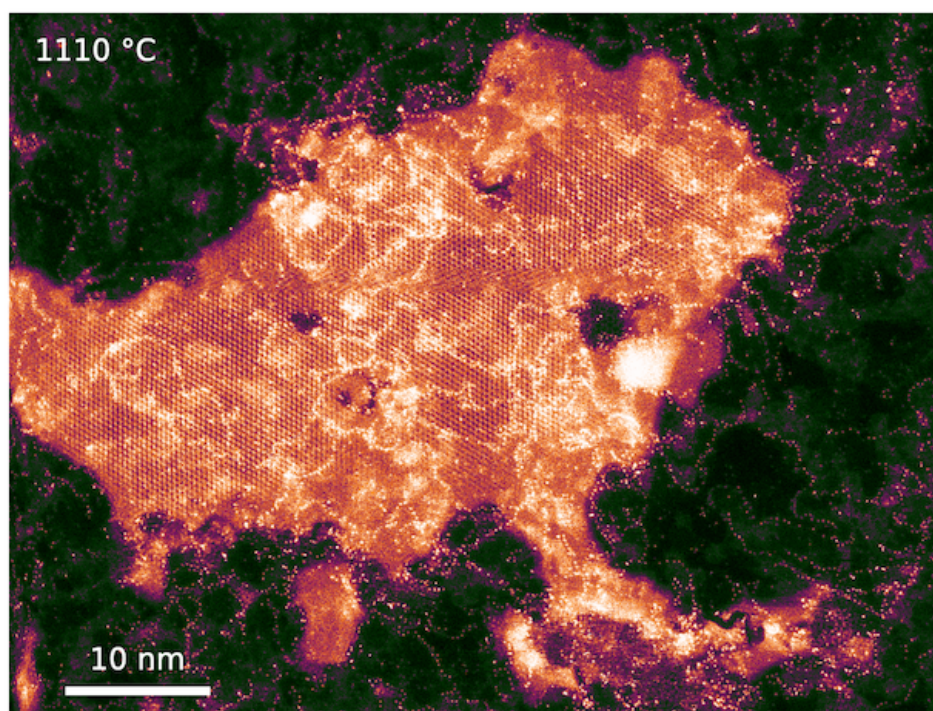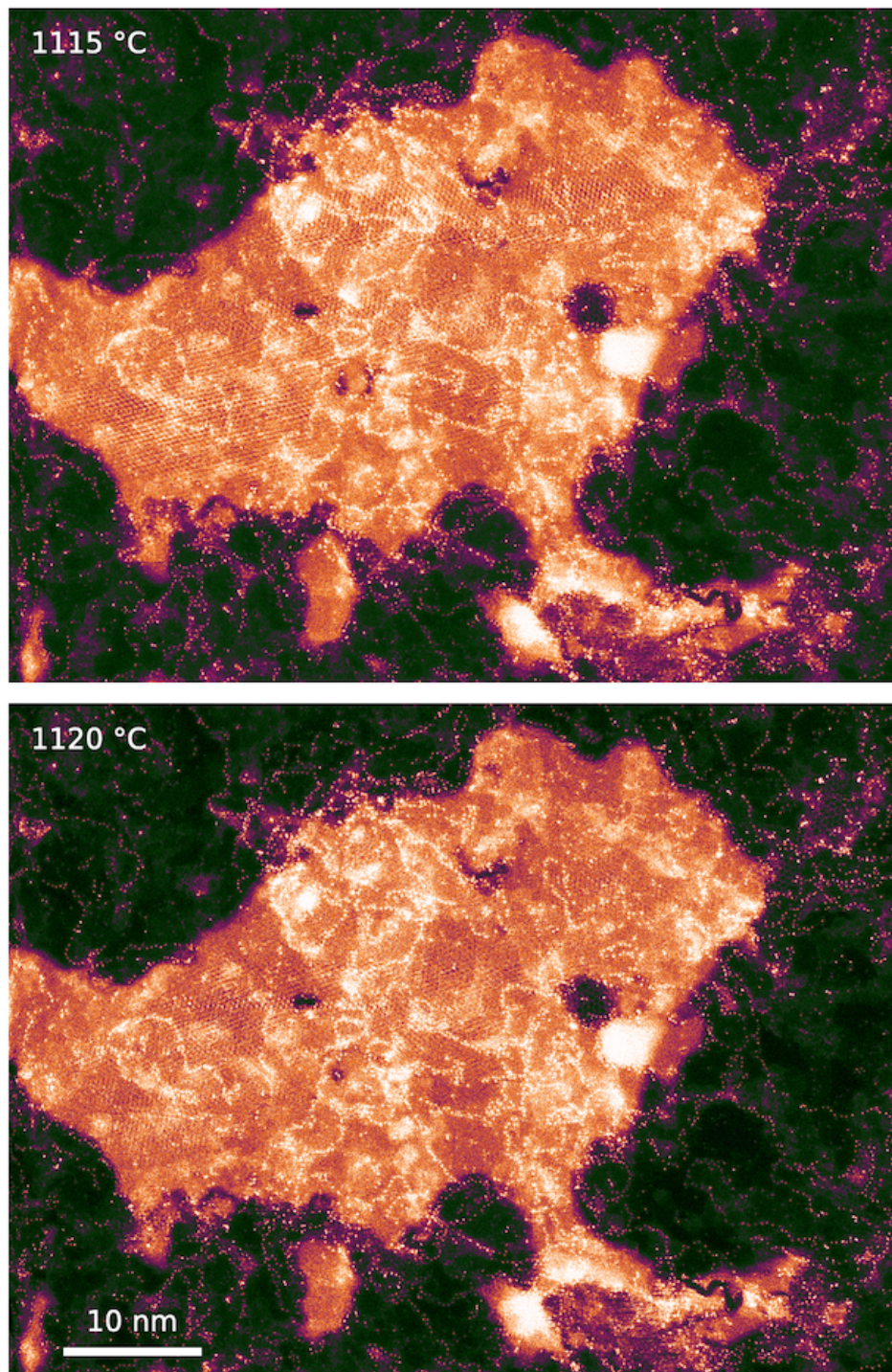
Figure S9: **1100°C and 1110°C**
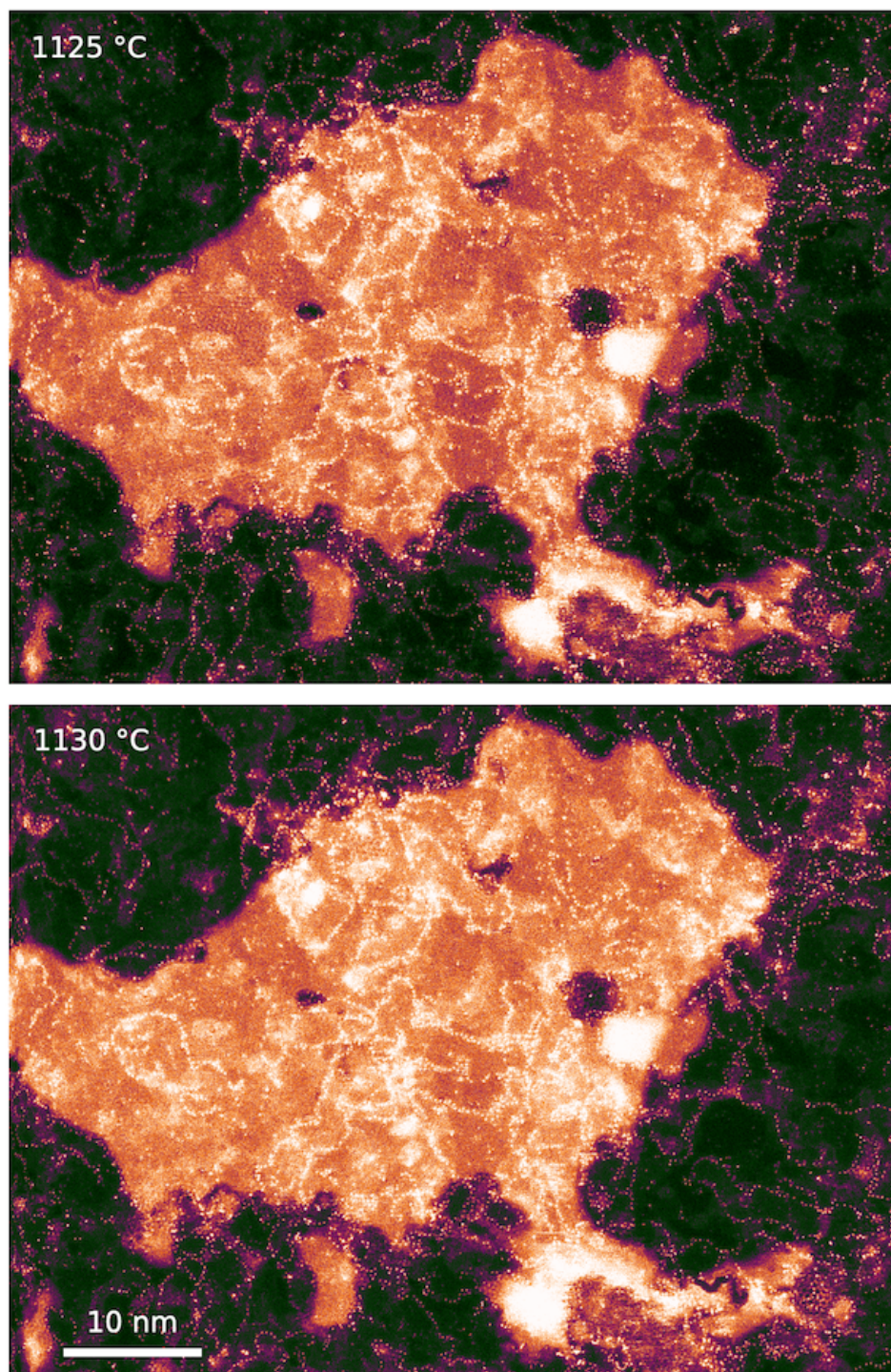
Figure S10: **1115°C and 1120°C**

Figure S11: **1125°C and 1130°C**

2D-Melting-Point Depression

At the nanometer scale, it is well established that the melting temperature of solids exhibits size dependence. This effect arises from differences in cohesive energy between surface and bulk atoms. For 3D nanoparticles, the melting temperature is inversely proportional to the square of the particle diameter or, equivalently, to the surface-to-volume ratio (*50*). In 2D particles, this scaling changes, reflecting the ratio of the circumference to the area, resulting in an inverse proportionality to the particle diameter (*51*). Figure S12 illustrates this relationship for various 2D AgI crystal sizes, with the x-axis representing the square root of the particle surface area. The surface area was determined from calibrated STEM ADF images using the ImageJ software suite. The experimental data in Figure S12 is fitted to the model

$$T_{m,2D} = T_{m,2D\infty} \left(1 - \frac{B}{\sqrt{A}} \right), \tag{Eq. S2}$$

where B and $T_{m,2D-\infty}$ are fitting parameters, and A is the area of the 2D particle. Based on this model, we estimate the 2D melting point for a crystal of infinite size, $T_{m,2D\infty}$, to be 1220±40°C.
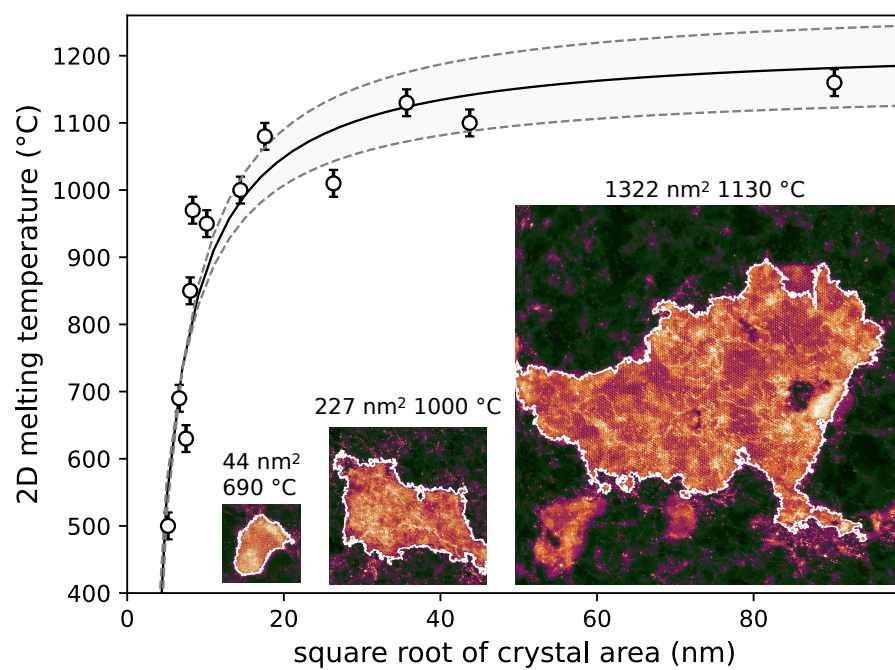
Figure S12: **Melting-point depression in 2D**. The insets show example STEM ADF images of crystals studied for the graph, and they are all displayed in the same scale. The solid line is the best fit to Eq. S2 and the dashed lines represent 95% confidence bounds of the fit.

Broadening of Diffraction Profiles in the Liquid Phase

Figure S13 shows averaged diffraction patterns and line profiles from the solid, hexatic and liquid phase. It is assumed that the FWHM measured in the solid phase is dominated by the intrinsic width as given by the NBED convergence angle, and additional broadening in the liquid and hexatic phase is added in quadrature. Hence, the broadening due to disorder in the liquid phase is estimated as

$$\Delta k_{liquid} = \sqrt{(\Delta k_{total})^2 - (\Delta k_{solid})^2}, \tag{Eq. S3}$$

which results in 1.66 nm^{-1} for the second order ring and 0.46 nm^{-1} for the first order ring. This means that the distance $(1/\Delta k)$ over which a periodicity and hence a correlation is present is ca. 0.6 nm for the periodicity of the second order peak (0.22 nm) and ca. 2 nm for that of the first order peak (0.38 nm).
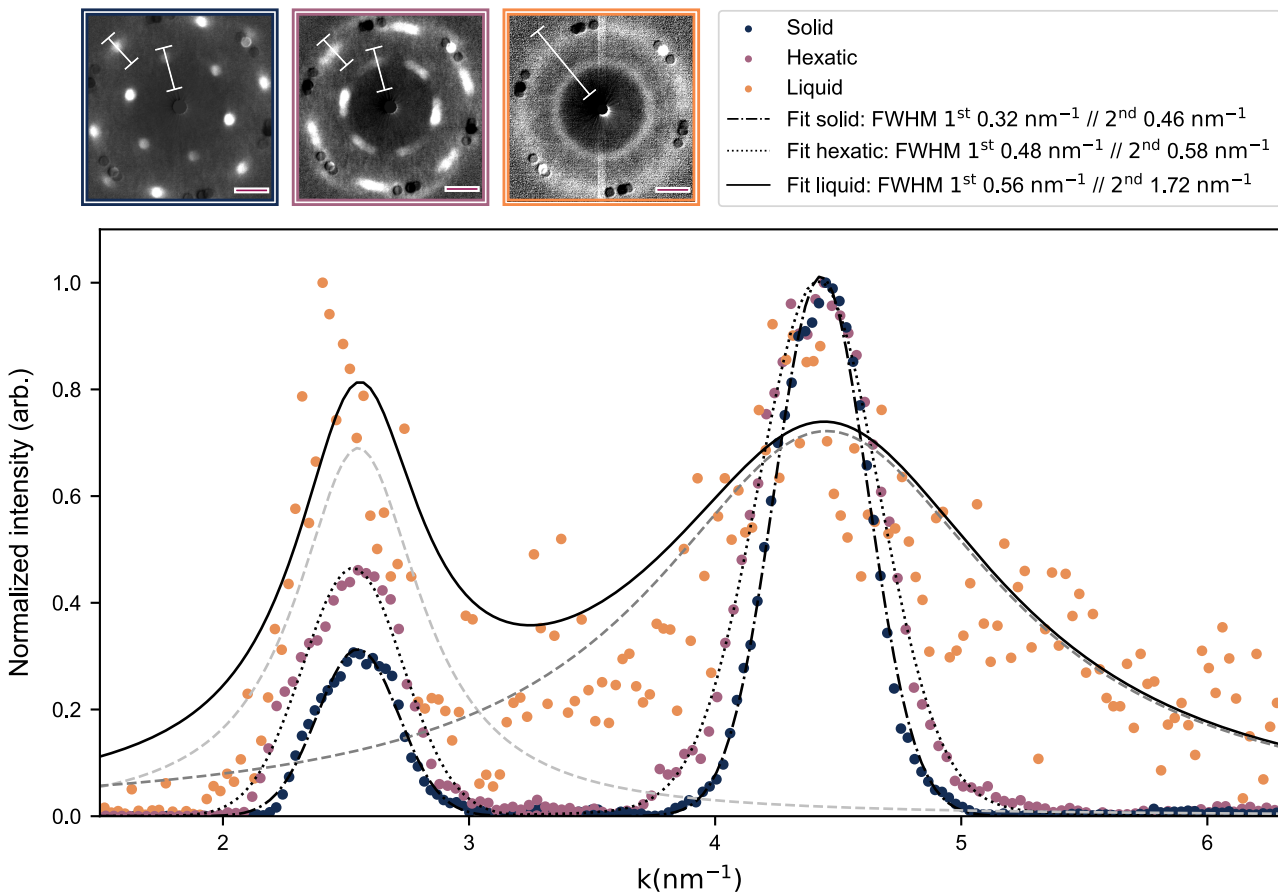
Figure S13: **Broadening of the diffraction features** Line profiles over the diffraction features in Figure 2 are analyzed to extract the full width at half maximum (FWHM) of each diffraction feature. The data is fitted using a sum of Gaussian and Cauchy-Lorentz line shapes (Voigt profile).

The Density of Isolated and Paired 5-7 Defects

The evolution of defects is visualized with Voronoi diagrams (Figure S14), highlighting defect structures in the data. The counts of 5-7 pairs, isolated dislocations (5-7 pairs surrounded by hexagons), and isolated disclinations (5- or 7-coordinated quasi-particles) are computed.

Below 1120°C, the defect density is low, dominated by vacancy-like defects (visualized in Voronoi diagrams as higher-order polygons surrounded by two or three 5-sided polygons) and 5-7-7-5 defects, which largely account for the observed 5-7 pairs. These defects have a zero Burgers vector, preserving long-range translational and orientational order. While some images show isolated dislocations, detailed analysis reveals that most 5-7 pairs are aligned in lines with a net zero Burgers vector (Figure S15). As the temperature approaches 1125°C, the defect density steadily increases, marking the transition to the hexatic phase. From 1125°C to 1140°C, isolated dislocation density rises sharply. Above 1140°C, 5-7 pairs increasingly form large defect clusters, reducing isolated dislocations. At lower temperatures, free disclinations are rare, but around 1135°C, the rise in isolated 5- and 7-quasi-particles signals the onset of the hexatic-to-liquid transition. The observed changes in defect densities and the unbinding of dislocation pairs near 1125°C align with KTHNY theory, which predicts dislocation unbinding at the solid-hexatic transition. While isolated dislocations unbinding into disclinations at the hexatic-liquid transition were not directly observed, the steady rise in isolated disclinations near this temperature supports the Kosterlitz-Thouless transition.

Finally, we point out that defect clustering introduces systematic ambiguity in the analysis of defects (*52*). For instance, a 5-7-5-7-5-7 defect cluster can be interpreted either as a paired dislocation combined with a single dislocation, or as three single dislocations. Our strict criteria of using only *completely* isolated defects reduces some of this ambiguity, but also underestimates the amount of dislocations and disclinations, in particular in the hexatic and liquid phases. Therefore, the result of Figure S14 should be considered an estimate that is useful primarily for qualitative analysis.
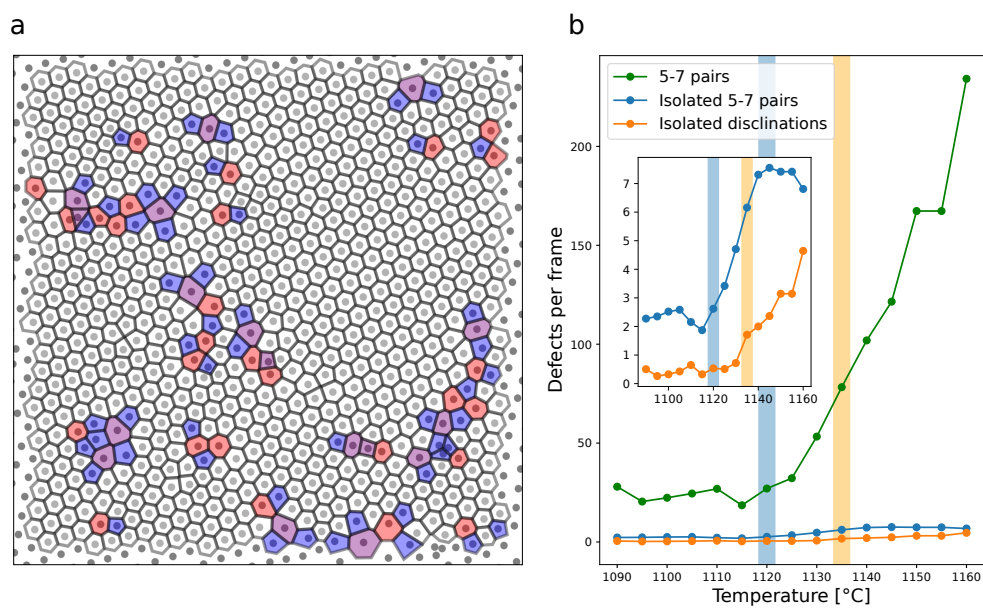
Figure S14: **a** Cutout of a Voronoi diagram of a single frame at 1135°C. Pentagons, heptagons and other not 6-sided polygons are colored in blue, red and purple, respectively. **b** The total amount of 5-7 pairs, isolated 5-7 pairs and isolated disclinations as a function of temperature. Note that the total amount of 5-7 pairs is scaled down by a factor of 10.
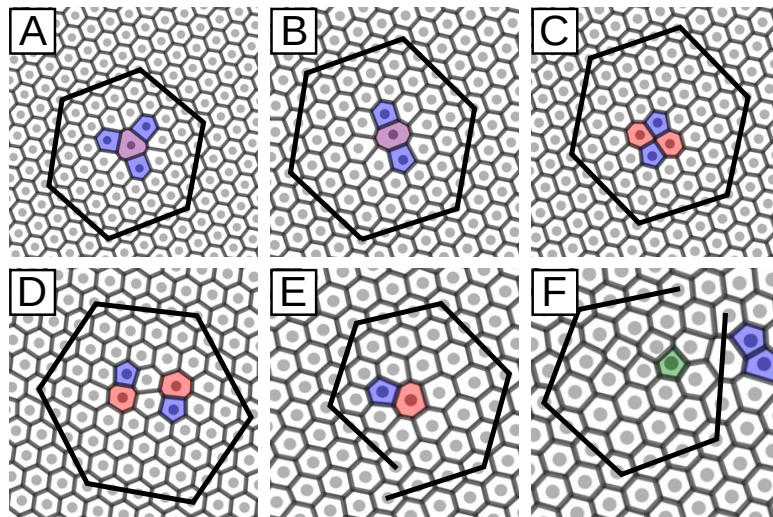
.

Burgers Vectors of Defects

Figure S15: **Burgers vectors of defects.** Vacancy-type defects **a-b**, as well as 5-7-7-5 **c** and paired 5-7 defects **d** have a zero Burgers vector, thus preserving long range order. Dislocations (isolated 5-7 defects) (E) and disclinations (F) have a non-zero Burgers vector which leads to decay of the translational and orientational order.
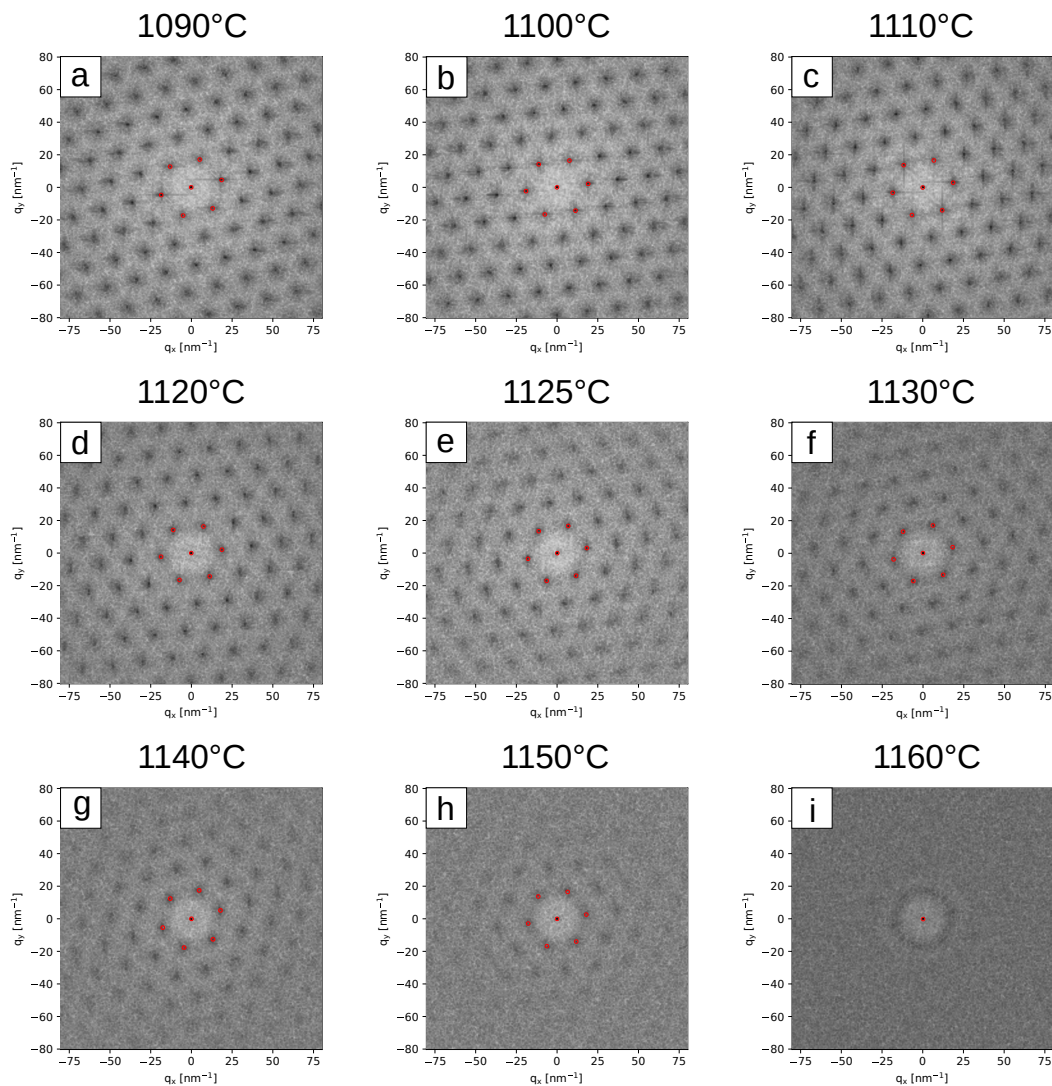
Structure Factors S(q)

Figure S16: **2D structure factors S(q)** The 2D structure factors of individual frames at different temperatures calculated using the freud.diffraction module (*35*). The red circles mark the center positions of the 2D Gaussian fits. **a-e** Solid phase; **f-h** hexatic phase; **i-j** liquid phase.

On Possible Sources of Residual Error

Vacancy-type defects with non-zero charge may induce slight in-plane distortions in AgI, potentially affecting the exponents of translational and rotational correlation decays (*48*). However, as our baseline data shows, these defects are not activated in significant quantities by the electron beam, nor is there any indication they would dominate at higher temperatures. Despite this, the slow decay of the translational correlation at low temperatures reveals that the 2D AgI is not a perfect hexagonal crystal system. Contributing factors to this behavior likely include crystal anisotropy (*24*) and out-of-plane distortions (*53*), similar to those observed in 2D CuI. In some cases, these issues caused severe correlation decay even at room temperature, leading to the exclusion of certain crystals from our analysis early on. Another potential source of uncertainty is the ambiguity in the fitting process for the correlation functions, yielding parameter values η_k and η_6 shown in Figure 3. However, the validity of the rotational correlation fit values is supported by the orientational parameter $|\Psi_6|$, which, based solely on hexagon positions and relative angles, exhibits behavior similar to η_6 (Figure 3). Finally, inaccurate determination of reciprocal lattice vectors can lead to large deviations in G_k (*54*), and as such, all images without a clear crystal direction or identifiable 1st-order peaks were discarded in our analysis. This approach, however, likely leads to an underestimation of the translational decay exponent values at higher temperatures.
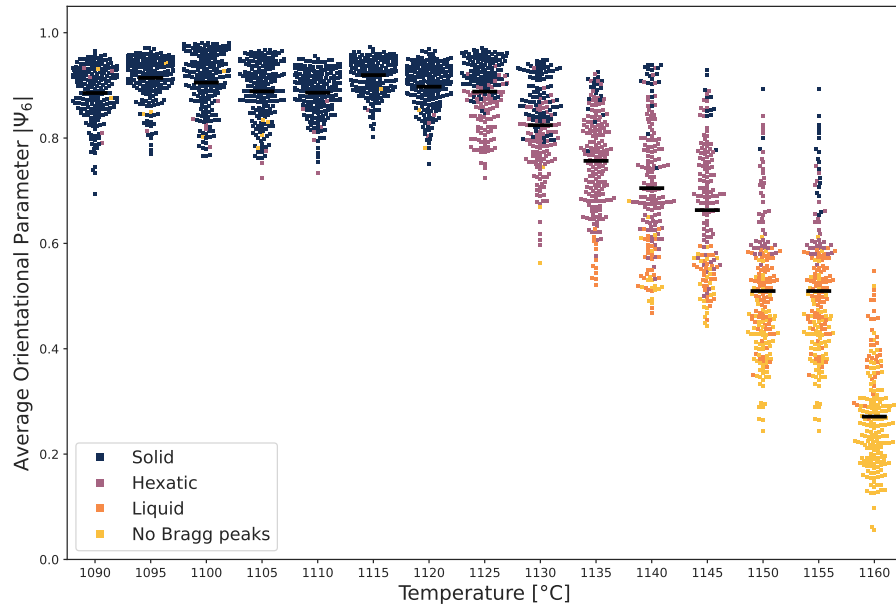
Orientational Parameters $|\Psi_6|$

Figure S17: **Orientational parameter** The average orientational parameter $|\Psi_6|$ as a function of temperature. The data points for the individual frames are color-coded according to the criteria described in Figure 3.
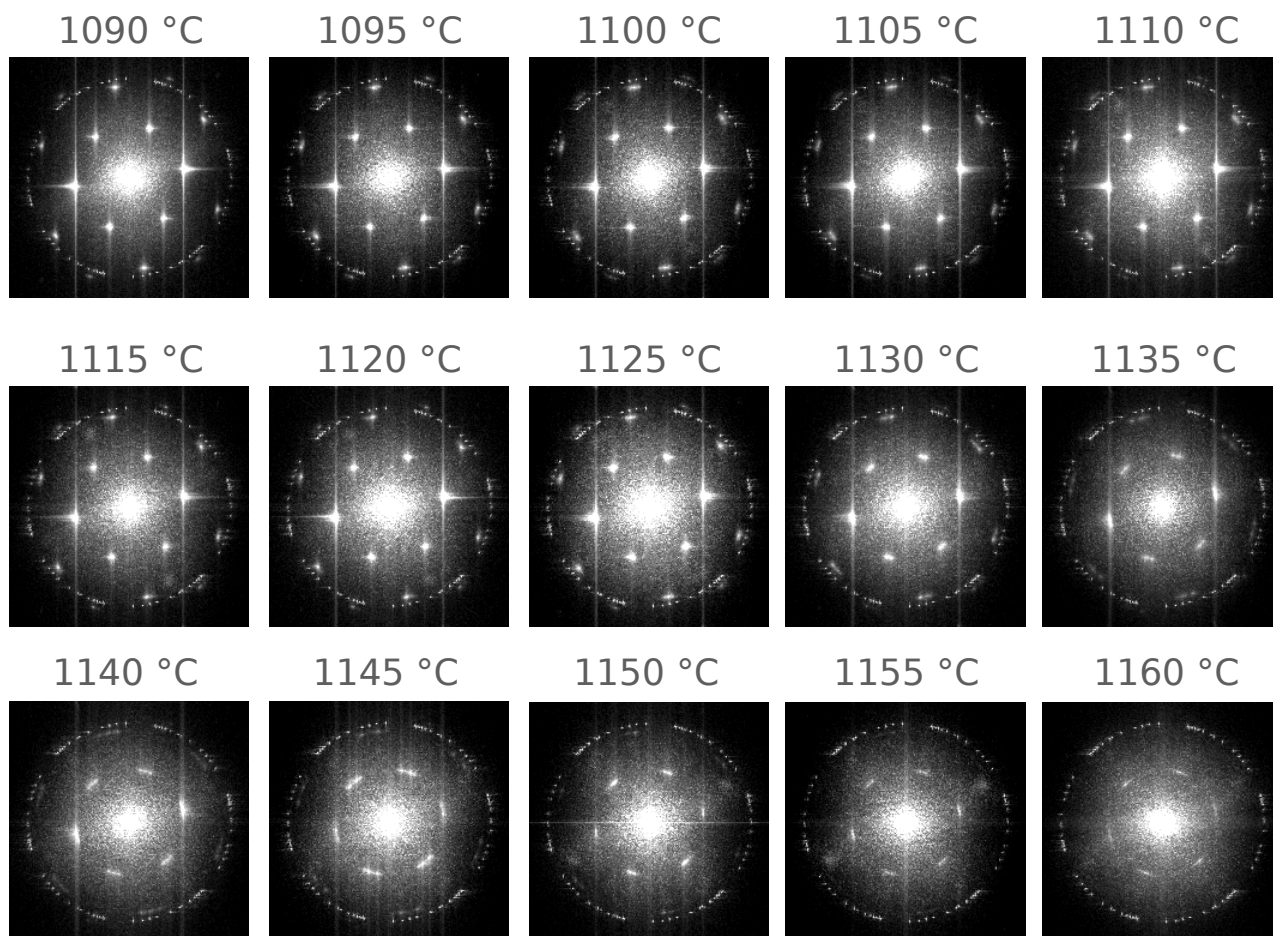
Supplementary Fourier Transforms

Figure S18: **Fourier transforms** Fourier transforms (FT) of the data that were used to compute the spatial correlation functions shown in Figure 3. Each FT consists of an average of 200 STEM ADF images.
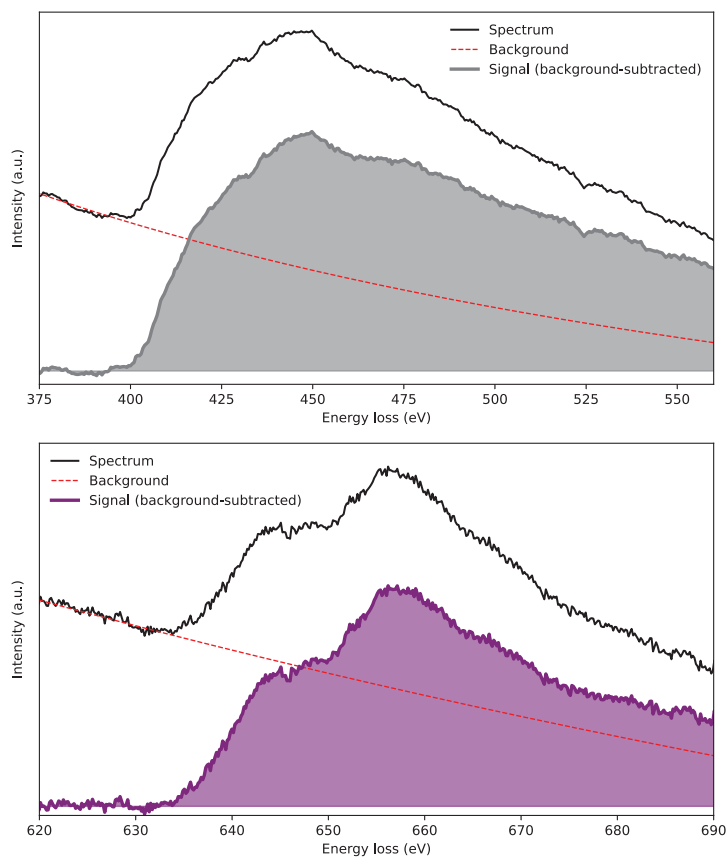
Electron Energy Loss Spectroscopy (EELS)

Figure S19: **Electron energy loss spectra of AgI** The Ag $M_{4,5}$ edge is shown on the top row and I $M_{4,5}$ edge on the bottom row.